



HAL
open science

Global ocean surface carbon product

Thi Tuyet Trang Chau, Marion Gehlen, Frédéric Chevallier

► **To cite this version:**

Thi Tuyet Trang Chau, Marion Gehlen, Frédéric Chevallier. Global ocean surface carbon product. [Research Report] CMEMS-MOB-QUID-015-008, Le Laboratoire des Sciences du Climat et de l'Environnement. 2021. hal-02957656v3

HAL Id: hal-02957656

<https://hal.science/hal-02957656v3>

Submitted on 24 Oct 2022 (v3), last revised 30 Nov 2022 (v4)

HAL is a multi-disciplinary open access archive for the deposit and dissemination of scientific research documents, whether they are published or not. The documents may come from teaching and research institutions in France or abroad, or from public or private research centers.

L'archive ouverte pluridisciplinaire **HAL**, est destinée au dépôt et à la diffusion de documents scientifiques de niveau recherche, publiés ou non, émanant des établissements d'enseignement et de recherche français ou étrangers, des laboratoires publics ou privés.



COPERNICUS
MARINE ENVIRONMENT MONITORING SERVICE

QUALITY INFORMATION DOCUMENT

QUALITY INFORMATION DOCUMENT

Global Ocean Surface Carbon Product

MULTIOBS_GLO_BIO_CARBON_SURFACE_REP_015_008

Issue: ~~1.2~~3.0

Contributors: Trang Chau, Marion Gehlen, Frédéric Chevallier

Approval date by the CMEMS product quality coordination team: 22/11/2021

CHANGE RECORD

| Issue | Date | § | Description of Change | Author | Validated by |
|-------|----------------|-----|---|--|--------------------|
| 0.0 | January 2019 | All | Creation of the document | Marion Gehlen, Thi Tuyet Trang Chau | Mercator Ocean |
| 1.0 | December 2019 | All | Update of the description: new methods (reconstruction and uncertainty quantification) and the corresponding validation | Thi Tuyet Trang Chau, Marion Gehlen, Frédéric Chevallier | Mercator Ocean |
| 2.0 | September 2020 | All | Update of the description and validation results corresponding to changes in: <ul style="list-style-type: none"> • input fields in reconstruction of surface ocean partial pressure of carbon dioxide, • parameterization of surface ocean downward mass flux of carbon dioxide (Wanninkhof 2014 instead of Wanninkhof 1992), uncertainty quantification of surface ocean pH. | Thi Tuyet Trang Chau, Marion Gehlen, Frédéric Chevallier | Stéphanie Guinehut |
| 3.0 | September 2021 | All | Update of the description and validation results corresponding to extensions of data coverage: <ul style="list-style-type: none"> • spatial extension towards the coasts and high latitudes (above 60°N) • temporal extension for the year 2020 | Thi Tuyet Trang Chau, Marion Gehlen, Frédéric Chevallier | Stéphanie Guinehut |

TABLE OF CONTENTS

| | |
|--|-----------|
| <i>Change Record</i> | 2 |
| <i>Table of contents</i> | 3 |
| <i>I Executive summary</i> | 4 |
| 1.1 Products covered by this document | 4 |
| 1.1 Summary of the results | 4 |
| 1.2 Estimated Accuracy Numbers | 7 |
| <i>II Production system description</i> | 8 |
| II.1 Origin of input fields | 8 |
| II.2 Description of system | 10 |
| <i>III Validation framework</i> | 12 |
| III.1 spco2 reconstruction | 12 |
| III.2 fgco2 reconstruction | 12 |
| III.3 Surface ocean pH reconstruction | 13 |
| <i>IV Validation results</i> | 14 |
| IV.1 spco2 reconstruction | 14 |
| IV.2 fgco2 reconstruction | 16 |
| IV.3 Surface ocean pH reconstruction | 18 |
| <i>V System's Noticeable events, outages or changes</i> | 20 |
| <i>VI Quality changes since previous version</i> | 21 |
| <i>VII References</i> | 24 |

I EXECUTIVE SUMMARY

I.1 Products covered by this document

This document presents approaches and tools used to produce and validate the Global Ocean Surface Carbon Product **MULTIOBS_GLO_BIO_CARBON_SURFACE_REP_015_008**.

| Short Description | Product code | Area | Delivery Time |
|-------------------|---|--------|---------------|
| Surface Carbon | MULTIOBS_GLO_BIO_CARBON_SURFACE_REP_015_008 | Global | Yearly |

The product provides surface ocean partial pressure of carbon dioxide, surface ocean downward mass flux of carbon dioxide expressed as carbon (positive for flux into the ocean) and surface pH on a regular grid (1°x1°) with a monthly resolution from 1985 onward.

I.1 Summary of the results

Surface ocean partial pressure of carbon dioxide (spco2) is obtained from an ensemble of feed forward neural networks (FFNNs) which is referred to as CMEMS-LSCE-FFNNv2 (Chau et al., 2021). The models were trained on 100 subsampled datasets from the Surface Ocean CO₂ Atlas (SOCAT) (<https://www.socat.info/>). Like the original data, subsamples are distributed after interpolation on 1° by 1° grid cells along ship tracks. Sea surface salinity, temperature, sea surface height, mixed layer depth, atmospheric CO₂ mole fraction, chlorophyll, spco2 climatology, latitude and longitude are used as predictors.

The CMEMS-LSCE-FFNNv2 approach follows a leave-*p*-out cross-validation (*p* spco2 observations corresponding to the month of reconstruction are excluded from the training data), allowing the quality of the reconstruction to be assessed against independent SOCAT data. At the global scale and over the full period of reconstruction (1985-2020), the root-mean-square difference (RMSD) is ~2.13 Pa, the mean absolute difference (MAD) is 1.28 Pa and the coefficient of determination (*r*²) is 0.76. CMEMS-LSCE-FFNNv2 quantifies spatial and temporal model uncertainties in terms of standard deviations of the 100-member ensembles.

The SOCAT database is an extensive compilation of surface carbon observations. The period covered by the reconstruction corresponds to a percentage larger than 85% of that data set. As shown in Figure 2, the spatial distribution of observations is, however, very heterogeneous and the data density remains poor over large areas of the global ocean (e.g., large areas of the Pacific Ocean, Indian Ocean) or seasonally biased (high latitudes). The approach ensures an optimal usage of available data but remains sensitive to data density.

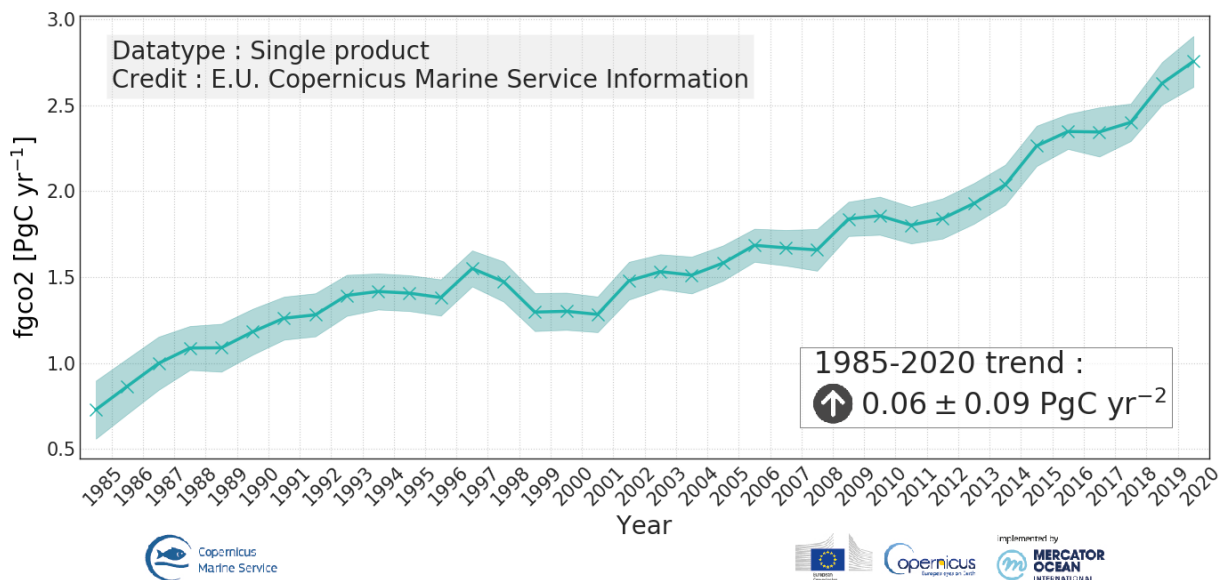
Surface ocean downward mass flux of carbon dioxide expressed as carbon (fgco2) was estimated using the gas exchange formulation $fgco2 = -k\rho L(1 - f_{sea\ ice})(spco2 - pCO_2^{atm})$, where *k* is the piston velocity, *ρ* is the seawater density, *L* is the temperature-dependent solubility of CO₂ and *f*_{sea ice} is the sea ice fraction.

The global ocean CO₂ sink corresponds to the global integral of fgco2 over space and time. In 2020 [resp. 2019], the global ocean CO₂ sink was 2.75±0.15 [resp. 2.63±0.12] PgC/yr (Figure 1). The number behind

the \pm sign corresponds to the standard deviation (σ) computed from the ensemble and it is thus an estimate of the uncertainty associated with the reconstruction. The average over the full period 1985-2020 is 1.62 ± 0.12 PgC/yr (including 0.15 ± 0.01 PgC/yr of the coastal uptake) with an interannual variability (temporal standard deviation) of 0.48 PgC/yr. Taking into account the total ocean area of 361,900,000 km² and the outgassing of river carbon of 0.78 PgC/yr yields an anthropogenic carbon uptake by the ocean of 3.65 ± 0.15 PgC/yr [3.51 ± 0.13 PgC/yr] for 2020 [2019], and 2.46 ± 0.15 PgC/yr averaged over the years 1985-2020. Our data-based estimates of the anthropogenic fluxes are above the estimates in Global Carbon Budget 2020 (GCB2020) by Friedlingstein et al. (2020) (see Table 5). The assessment in GCB2020, however, pointed out that the models might underestimate the global ocean CO₂ sink. In Hauck et al. 2020, the authors also suggested that further studies are needed to understand the model-data mismatch and to improve the riverine carbon inputs.

Surface ocean pH on total scale (pH) was computed from spco2 and reconstructed surface ocean alkalinity using the CO2sys speciation software (Van Heuven et al., 2011; Lewis and Wallace, 1998). Time and space varying alkalinity fields were obtained from a multivariate linear regression with salinity, temperature, dissolved silica and nitrate (Table 2) as independent variables. pH decreases in response to the uptake of CO₂ by the ocean. The rate of decrease computed over the period of reconstruction is 0.0016 pH units (Figure 1). The global RMSD between pH from GLODAPv2.2021 bottle data and the reconstructed pH over the period 1985-2020 is 0.0348 pH units and the r^2 values is 0.5730.

Global integrated surface downward flux of total CO₂



Yearly mean surface sea water pH reported on total scale

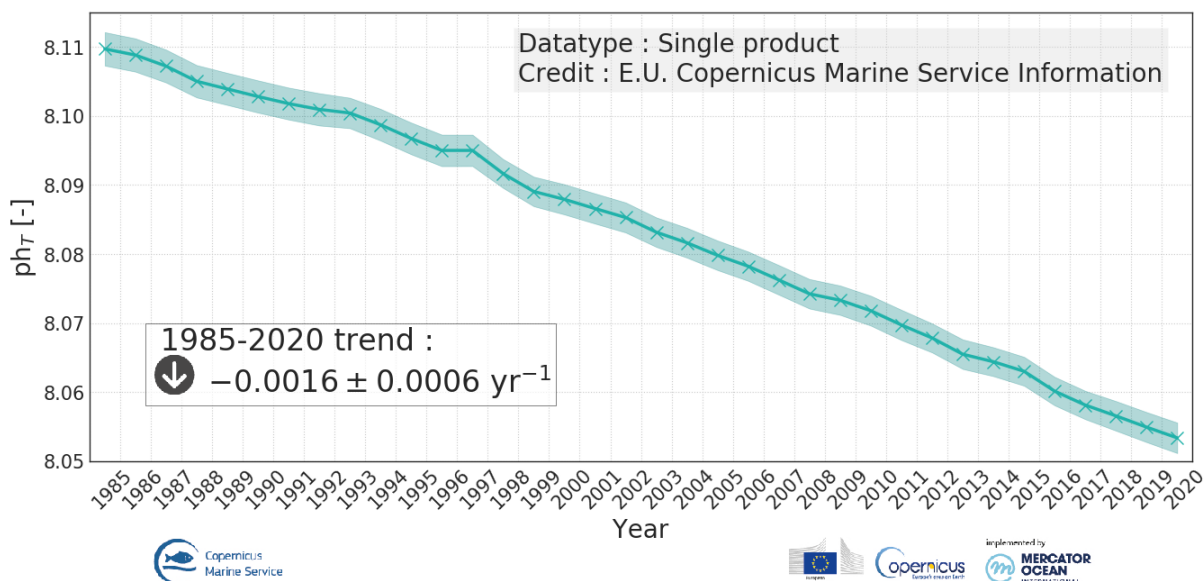


Figure 1. Top: area integrated yearly surface downward flux of total CO₂ for the period from 1985 onward (GLOBAL_OMI_HEALTH_CARBON_co2_flux_integrated product). Bottom: yearly mean surface pH reported on total scale (GLOBAL_OMI_HEALTH_CARBON_ph_area_averaged CMEMS product). The uncertainty envelop is defined as the 68% confidence interval (estimate ± uncertainty) of yearly means. The trend and its variation are computed as the mean and standard deviation of the differences between consecutive estimates.

I.2 Estimated Accuracy Numbers

The quality of the reconstruction is assessed against independent SOCAT data in a leave- p -out cross-validation where p spco2 observations corresponding to a given month of reconstruction have been excluded from the training data. A ratio of 2:1 for training and validating is used. At the global scale and over the full period of reconstruction (1985-2020), the main statistics are reported in the following table.

For pH, the statistics are with respect to the independent GLODAPv2.2021 bottle data over the period 1985-2020 (<https://www.glodap.info/index.php/merged-and-adjusted-data-product-v22021/>).

Table 1: Estimated skill over the global, open, and coastal oceans (see section III for definitions).

| Variable | | Metrics | | | Units |
|----------|---------|---------|--------|--------|----------------|
| | | MAD | RMSD | r^2 | |
| spco2 | global | 1.28 | 2.13 | 0.76 | Pa |
| | open | 1.15 | 1.86 | 0.77 | |
| | coastal | 2.41 | 3.72 | 0.70 | |
| ph | global | 0.0193 | 0.0348 | 0.5730 | pH total scale |
| | open | 0.0173 | 0.0296 | 0.6061 | |
| | coastal | 0.0531 | 0.0836 | 0.4045 | |

II PRODUCTION SYSTEM DESCRIPTION

Production centres name: Laboratoire des Sciences du Climat et de l'Environnement (LSCE) (MULTIOBS-LSCE-GIF-FR)

II.1 Production system name: CMEMS-LSCE-FFNNv2Origin of input fields

Table 2: Details of input fields

| Reconstruction of surface ocean CO ₂ partial pressure | | |
|--|--|---|
| Target data: surface ocean CO ₂ partial pressure. | | |
| Measurements of CO ₂ fugacity | Bakker et al., 2016 | SOCATv2021: https://www.socat.info/ (last access 16/06/2021) |
| Predictor data | | |
| Sea surface temperature | CMEMS CMEMS | MULTIOBS_GLO_PHY_TSUV_3D_MYNRT_015_012 (1993-2020) SST_GLO_SST_L4_REP_OBSERVATIONS_010_011 (1985-1992) |
| Sea surface salinity | CMEMS | MULTIOBS_GLO_PHY_TSUV_3D_MYNRT_015_012 (1993-2020) Climatology (1985-1992) computed from MULTIOBS_GLO_PHY_TSUV_3D_MYNRT_015_012 (1993-2020) |
| Sea surface height | CMEMS | MULTIOBS_GLO_PHY_TSUV_3D_MYNRT_015_012 (1993-2020) Climatology plus linear trend (1985-1992) computed from MULTIOBS_GLO_PHY_TSUV_3D_MYNRT_015_012 (1993-2020) |
| Mixed layer depth | Menemenlis et al., 2008 | ECCO2: "Estimating the Circulation and Climate of the Ocean" project Phase II (1992-2020) Climatology (1985-1991) computed from ECCO2 (1992-1997) |
| Chlorophyll | GlobColour, available from CMEMS | http://www.globcolour.info/products_description.html (1998-2020) Climatology computed from GlobColour (1985-1997) |
| Atmospheric CO ₂ mole fraction | Chevallier et al. 2005, 2010; Chevallier, 2013 | CO ₂ atmospheric inversion from the Copernicus Atmosphere Monitoring Service (https://atmosphere.copernicus.eu/) |
| spco2 climatology | Takahashi et al. (2009) | LDEO spco2 climatology https://www.pmel.noaa.gov/co2/story/LDEO+Surface+Ocean+CO2+Climatology |

| Reconstruction of surface ocean downward mass flux of CO ₂ | | |
|---|--|---|
| 6-hourly wind speed | ERA5 | https://www.ecmwf.int/en/forecasts/datasets/reanalysis-datasets/era5 |
| Atmospheric CO ₂ mole fraction | Chevallier et al. 2005, 2010; Chevallier, 2013 | CO ₂ atmospheric inversion from the Copernicus Atmosphere Monitoring Service (https://atmosphere.copernicus.eu/) |
| Total pressure | ERA5 | https://www.ecmwf.int/en/forecasts/datasets/reanalysis-datasets/era5 |
| Sea ice fraction | CMEMS | SST_GLO_SST_L4_REP_OBSERVATIONS_010_011 SST_GLO_SST_L4_NRT_OBSERVATIONS_010_001 |

| Reconstruction of surface ocean pH on total scale | | |
|---|---|---|
| Nitrate, dissolved silica | World Ocean Atlas v2 2018 | https://www.ncei.noaa.gov/data/oceans/woa/WOA18/ |
| pH (validation data) | GLODAPv2.20 21 bottle data (Lauvset et al 2021) | https://www.glodap.info/index.php/merged-and-adjusted-data-product-v22021/ |

In addition to the predictors listed in this table, latitude and longitude are also used as predictors for the reconstruction of surface ocean pCO₂.

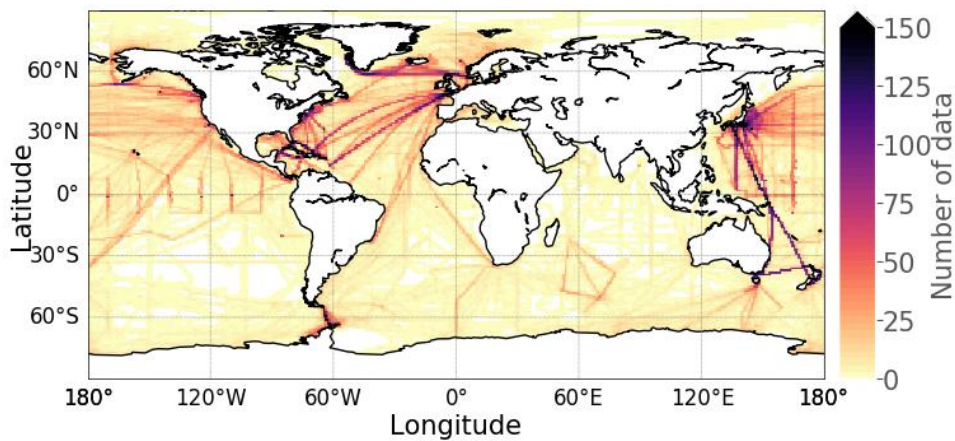


Figure 2 Distribution of SOCAT v2021 – ship traces for the period Jan 1985-Dec 2020 (Bakker et al., 2016). Monthly data on 1°x1° regular grid.

II.2 Description of system

(a) Reconstruction of surface ocean carbon dioxide partial pressure

Central to the production process is the reconstruction of surface ocean carbon dioxide partial pressure (spco2) by a Feed Forward Neural Network (FFNN) model following an ensemble-based approach (Chau et al. 2021). Taking advantage of the Surface Ocean CO₂ Atlas (SOCAT) (Bakker et al., 2016), the ensemble-based FFNN approach is used to reconstruct the global distribution of spco2 with a monthly resolution over the global 1°×1°-gridded surface ocean. FFNN models were fitted on 100 datasets sub-sampled randomly from the drivers and SOCAT data with a ratio of 2:1 for training and validating. The model is sensitive to the observational coverage. This limitation is partly overcome by the FFNN approach as the reconstruction of monthly global ocean distributions draws on a larger data set such that FFNN outputs remain close to realistic values. The approach further uses observations in a 3-month gliding window centered on the month of reconstruction. Note that the data from the month of reconstruction is excluded from the training data in order to reduce model overfitting. The new network was developed at the *Laboratoire des Sciences du Climat et de l'Environnement* (LSCE) and validated as an improvement of LSCE-FFNN-v1 (Denvil-Sommer et al. 2019). The model outputs are part of the Copernicus Marine Environment Monitoring Service (CMEMS). It is hence referred to CMEMS-LSCE-FFNNv2.

The means (μ) and standard deviations (σ) are computed from the 100-member ensembles for each of the three variables contributing to the global carbon product. The standard deviation stands for the associated model uncertainty. In this report, the notation $\mu \pm \sigma$ expresses an estimate of the surface ocean partial pressure of CO₂ (as well as surface ocean downward mass flux of CO₂ or pH) along with its relative uncertainty. In cases of the uncertainty reported for the spatial mean and/or temporal mean of carbon variables, spatial and temporal decorrelation length scales are used to reduce the bias in variance estimates of the mean quantities.

(b) Reconstruction of surface ocean downward mass flux of carbon dioxide expressed as carbon

The surface ocean downward mass flux of CO₂ is computed from the gas exchange formulation $fgco2 = -k\rho L(1 - f_{sea\ ice})(spco2 - pCO_2^{atm})$

where k is the piston velocity, ρ the seawater density, L is the temperature-dependent solubility of CO₂ (Weiss, 1974) and $f_{sea\ ice}$ is the sea ice fraction. The piston velocity is estimated after Wanninkhof (2014) with wind speed computed from 6-hourly ERA5 wind speed and the sea ice fraction extracted from OSTIA data. $spco2$ corresponds to the surface ocean pCO₂, reconstructed by the neural network CMEMS-LSCE-FFNNv2 model and pCO₂^{atm} was derived from the atmospheric CO₂ mixing ratio fields provided by the CAMS inversion (Chevallier et al. 2005, 2010; Chevallier 2013).

The uncertainty of the surface downward mass flux is quantified after applying the gas exchange formula to the difference between the 100-member ensemble of monthly spco2 estimates and the corresponding atmospheric pCO₂ values.

(c) Reconstruction of surface ocean pH

Surface ocean pH is calculated from reconstructed spco2 and alkalinity using the speciation software CO2sys (Van Heuven et al., 2011; Lewis and Wallace, 1998). Time and space varying surface ocean alkalinity fields are obtained from the multivariate linear regression model LIAR (Carter et al., 2016;

2018) as a function of sea surface temperature and salinity, as well as climatological nitrate and dissolved silica from World Ocean Atlas v2018 (<https://www.ncei.noaa.gov/data/oceans/woa/WOA18/>). Uncertainties of input fields are taken as constant in time but spatially variable. For temperature and salinity, the uncertainty is defined as the RMSD between the products and observations, and for the nitrate and dissolved Si climatologies the uncertainties are defined as 15% of the values (see <https://archimer.ifremer.fr/doc/00651/76336/77327.pdf>).

Total uncertainty of the monthly output fields ($\sigma_{\text{tot}, m}$) is evaluated by taking into account empirical variances of two sources: model randomness ($\sigma_{\text{ran}, m}$) and systematic errors ($\sigma_{\text{sys}, m}$):

$$\sigma_{\text{tot}, m}^2 = \sigma_{\text{ran}, m}^2 + \sigma_{\text{sys}, m}^2$$

The first uncertainty represents the dispersion of the pH field computed from 100 ensemble members of the reconstructed spco2, and the latter is assessed through uncertainty propagation following Orr et al. (2018) and the speciation software CO2sys (Lewis and Wallace, 1998; Van Heuven et al., 2011). Inputs to the uncertainty propagation routine are default values for dissociation constants, measurement errors, uncertainty estimates for alkalinity fields from LIAR (Carter et al., 2016; 2018), and reconstruction errors between of spco2 estimates from the CMEMS-LSCE-FFNNv2 approach and SOCAT observations.

III VALIDATION FRAMEWORK

III.1 spco2 reconstruction

Only two thirds of the SOCAT target data are used for the training algorithm, leaving one third for model validation. The models are trained separately for each month, resulting in adaptive models with a common architecture but trained on different data. To increase the amount of data available for training, the models are trained using as target data from a 3-month moving window of the entire period from 1985 onward but excluding the reconstructed month.

Model output is assessed on the independent SOCAT data and collocated reconstructed data. A leave- p -out cross-validation approach is applied (where p is the amount of data in the month considered for reconstruction) and 100 random subsamples of independent data are drawn from the SOCAT dataset. The network was run on each subsample. From these 100 results the mean was chosen as an estimate of monthly spco2 per grid cell.

All metrics are computed over the full reconstruction period and the sub-period (2001-2016) for the comparison with the LSCE-FFNN-v1 (see section VI). The assessment is broken down into the regions defined after Gurney et al. (2008) with modification from Landschützer et al. (2014) (Table 13 and Figure 3). Reconstructed data along the coast are evaluated within the coastal zones defined from the MARGins and CATchments Segmentation (MARCATS; Laruelle et al. 2013) and collocated on the 1°x1° SOCAT grid.

III.2 fgco2 reconstruction

There is no independent data for validating fgco2. CMEMS-LSCE-FFNNv2 estimates of air-sea CO₂ fluxes are assessed by comparison to published estimates derived from an ensemble of global ocean biogeochemical models (GOBMs) used in the Global Carbon Project (GCP, Friedlingstein et al., 2020). Note that in order to obtain estimates for the anthropogenic fluxes the data-based estimates need to be corrected for the preindustrial outgassing of riverine carbon input (0.78 PgC/yr, Resplandy et al., 2018).

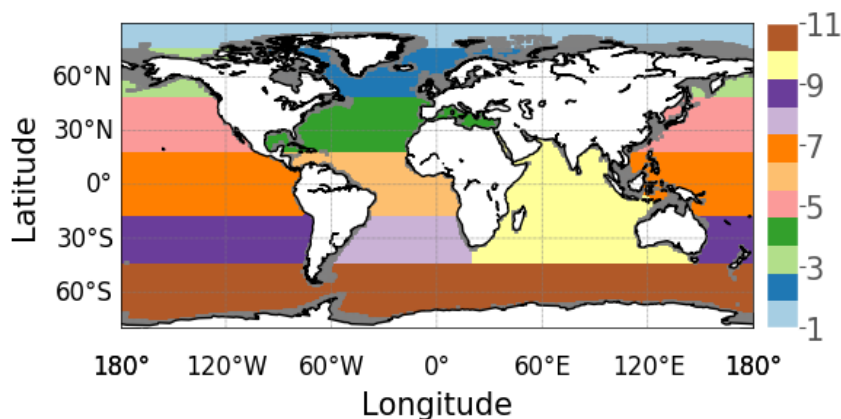


Figure 3. Map of the Ocean Inversion regions (Gurney et al. 2008, modified by Landschützer et al., 2014) used for model assessment. The coastal mask (grey) is defined with the MARGins and CATchments Segmentation (MARCATS; Laruelle et al, 2013) collocated on 1°x1° SOCAT grid.

| Number | Name |
|--------|----------------------|
| 1 | Arctic |
| 2 | Subpolar Atlantic |
| 3 | Subpolar Pacific |
| 4 | Subtropical Atlantic |
| 5 | Subtropical Pacific |
| 6 | Equatorial Atlantic |
| 7 | Equatorial Pacific |
| 8 | South Atlantic |
| 9 | South Pacific |
| 10 | Indian Ocean |
| 11 | Southern Ocean |

Table 3: Ocean Inversion regions (Gurney et al. 2008, modified by Landschützer et al., 2014)

III.3 Surface ocean pH reconstruction

The pH from GLODAPv2.2021 bottle data (<https://www.glodap.info/index.php/merged-and-adjusted-data-product-v22021/>) are used for the evaluation of reconstructed surface ocean pH during 1985-2020. Only data from depths shallower than 10 m are used. Data are averaged per month and on a regular 1°x1° grid, which resulted in 10813 data points. The reconstruction metrics are calculated from co-located reconstructed values at these data points.

IV VALIDATION RESULTS

IV.1 spco2 reconstruction

| Region | Latitude boundaries | MAD (Pa) | | RMSD (Pa) | | r ² | |
|---|---------------------|----------|---------|-----------|---------|----------------|---------|
| | | Open | Coastal | Open | Coastal | Open | Coastal |
| Global (287984, 33864) | | 1.15 | 2.41 | 1.86 | 3.72 | 0.77 | 0.70 |
| Subpolar Atlantic (25705, 13749) | 49°N to 76°N | 1.46 | 2.16 | 2.43 | 3.19 | 0.77 | 0.80 |
| Subpolar Pacific (11575, 4145) | 49°N to 76°N | 2.04 | 4.03 | 2.92 | 5.52 | 0.65 | 0.57 |
| Equatorial Pacific (47893, 258) | 18°S to 18°N | 1.11 | 1.90 | 1.74 | 2.69 | 0.79 | 0.47 |
| South Pacific (18396, 1276) | 44°S to 18°S | 0.81 | 0.95 | 1.21 | 1.44 | 0.74 | 0.62 |
| Southern Ocean (31760, 5798) | 90°S to 44°S | 1.27 | 2.51 | 1.96 | 3.60 | 0.61 | 0.64 |

Table 4: Statistical validation for CMEMS-LSCE-FFNNv2 over the period 1985-2020. Comparison between reconstructed surface ocean spco2 and spco2 values from the SOCAT data that were not used during the algorithm training. Global statistics and regional examples (Figure 3), number of measurements of SOCATv2021 per (open, coastal) region between brackets.

Table 4 exemplifies skill scores computed for 5 regions. It illustrates - for the full period - that the highest RMSDs (open: 2.92 Pa, coastal: 5.52 Pa) and MAD (open: 2.04 Pa., coastal: 4.03 Pa) are associated with the region having the lowest data density and high temporal and/or spatial pCO₂ variations (e.g., Subpolar Pacific, 15720 observations). The CMEMS-LSCE-FFNNv2 reconstruction over the coastal regions for the full period is roughly twice less effective than over the open ocean in terms of RMSD and MAD while it shows a rather good fit with r² = 0.70. The high RMSD reflects local high model errors along the continental shelves (Figure 5) which are characterized by complex physical and biological dynamics leading to high variability at small scales. Further model improvement is needed in order to capture such high spatial and temporal variability of surface ocean pCO₂ present in observations (see in Bakker et al. 2016; Laruelle et al., 2017, and references therein). An in-depth analysis on the model reconstruction over different oceanic basins for both open and coastal regions is presented in Chau et al. 2021.

The average surface ocean spco2 for the period 1985-2020 is shown on the left panel of Figure 4. High surface ocean spco2 values are associated to the upwelling of deep water, which is naturally enriched in DIC (Dissolved Inorganic Carbon, e.g., Equatorial Pacific upwelling). Low CO₂ partial pressures are found in cold northern and southern latitudes, a combination of the temperature effect on the solubility of CO₂ and the drawdown of DIC by biological activity. The spatial uncertainty of spco2 corresponding to the standard deviation of outputs from the 100 models from the CMEMS-LSCE-FFNNv2 is displayed on the right plots of Figure 4. These maps illustrate the confidence level in the reconstruction of spco2. Large estimates of the uncertainties were found in the coastal regions, regions sparse or devoid of SOCAT data (see Figure 2) such as Indian Ocean, Southern Ocean, and regions with high or low surface pressure of CO₂ such as East Pacific, Labrador Sea, North Western Pacific.

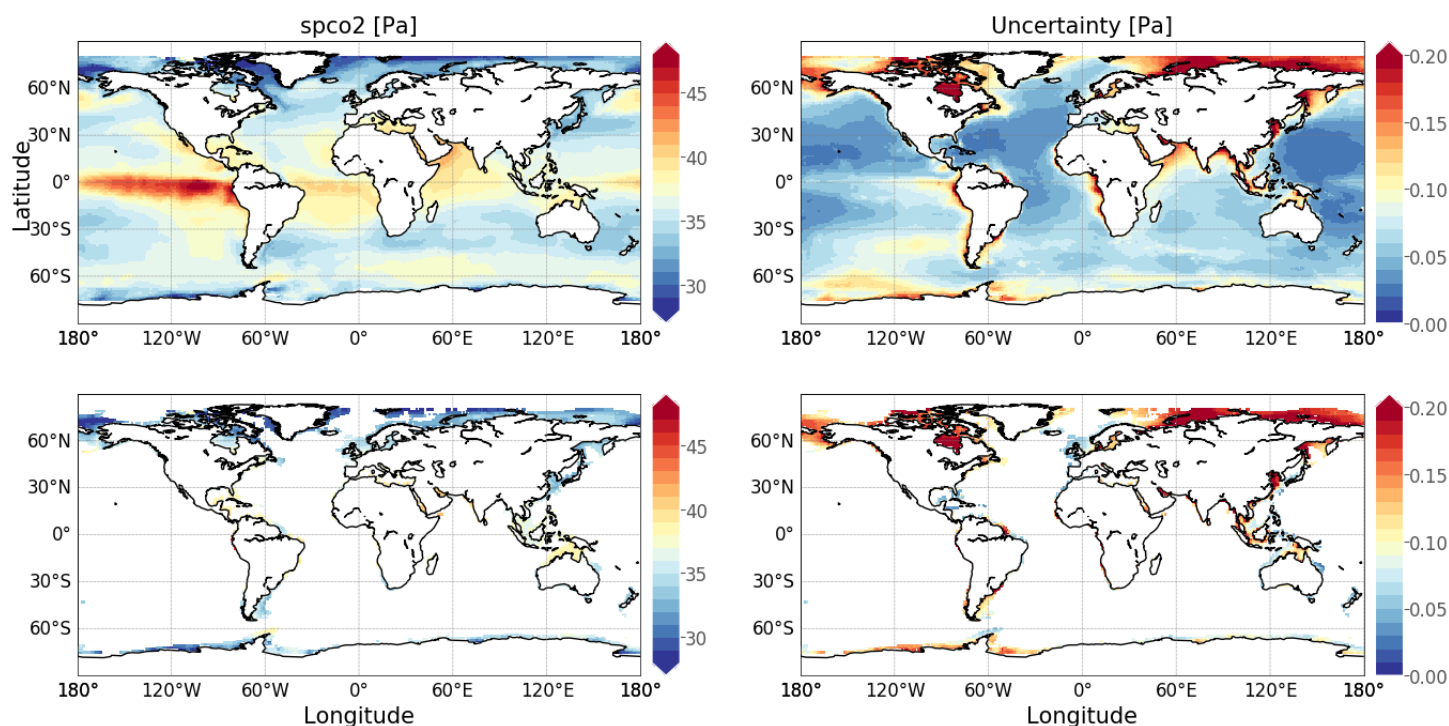


Figure 4. Reconstructed surface ocean carbon dioxide partial pressure averaged over over the global ocean (top) and coasts (bottom) for 1985 to 2020. Mean (left) and standard deviation (right) of the 100-member CMEMS-LSCE-FFNNv2 model outputs are shown. The uncertainty estimate of the temporal mean per grid cell was corrected with a constant decorrelation length scale of 3 months.

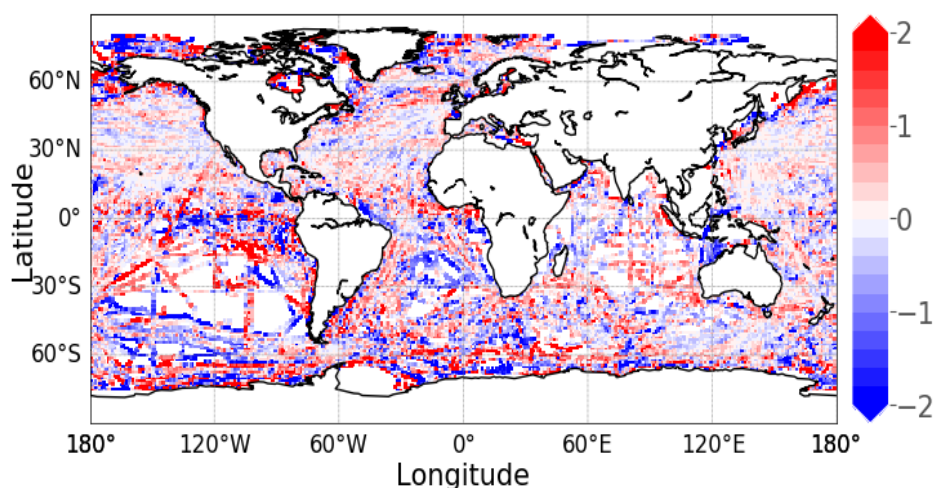


Figure 5. Map of the mean differences between MULTIOBS spco2 and the entire SOCAT dataset [Pa].

While the average bias of reconstructed surface ocean partial pressure compared to the SOCAT data is small, there are areas with persisting strong positive or negative biases (e.g., coastal seas and continental shelves, subpolar and polar regions, Eastern Pacific Ocean, Western South Atlantic). Figure 5 shows the full dataset of the differences from the observations for the period 1985-2020. It hides the still sparse data coverage for individual months, which challenges any reconstruction method. Even more problematic is the poor data coverage of large regions (e.g., coasts, high latitudes, Indian Ocean and

South Pacific Ocean). Reconstructed monthly fields are very noisy with high uncertainty over areas with poor data coverage (see Figure 2) and/or high variations of pCO₂, and should be viewed with caution.

IV.2 fgco2 reconstruction

Table 5 presents a comparison between CMEMS-LSCE-FFNNv2 and an ensemble of global ocean biogeochemical general circulation models (GOBMs) used in Global Carbon Budget 2020 (GCB2020, Friedlingstein et al. 2020) for the reconstruction of air-sea CO₂ fluxes. The global ocean CO₂ sink corresponds to the global integral of fgco2 over space and time. The reconstructed field covers both the open ocean and coastal regions and hence approximately 96.15% of the total ocean area (361,900,000 km²). In 2020 [resp. 2019], the global ocean CO₂ sink was 2.75±0.15 [resp. 2.63±0.12] PgC/yr (Figure 1). The average of yearly contemporary fluxes over the full period 1985-2020 is 1.62±0.12 PgC/yr (including 0.15±0.01 PgC/yr from the coastal uptake) with an interannual variability (temporal standard deviation) of 0.48 PgC/yr. Taking into account the total ocean area of 361,900,000 km² and the outgassing of river carbon of 0.78 PgC/yr yields an anthropogenic carbon uptake by the ocean of 3.65±0.15 PgC/yr [3.51±0.13 PgC/yr] for 2020 [2019] and 2.46 ±0.15 PgC/yr for the years 1985-2020. Our data-based estimates of the anthropogenic uptake are above the model-based estimates by Friedlingstein et al. (2020) (see Table 5). However, it is demonstrated in Friedlingstein et al. (2020) and Hauck et al. (2020) that the CMEMS-LSCE-FFNNv2 flux estimates are in line with alternative data-based estimates. The spatial distribution of CO₂ sources and sinks, as well as decadal trends of data-based and model-based estimates are consistent at global and regional scales. However, the mismatch in magnitude of these estimates and uncertainty from global scaling and river flux adjustment are still large and remain to be resolved.

The new ensemble-based approach yields spatio-temporal varying uncertainties which are consistent with uncertainty estimates of an ensemble of data-based and model-based approaches in Hauck et al. (2020). However, they are lower than the previous GCB published total estimate of ± 0.6 PgC/yr. The latter estimate corresponds to the mean of flux estimates from global ocean biogeochemical general circulation models (GOBMs). The uncertainty estimate combines the interannual variability derived from GOBMs (± 0.4 PgC/yr) and the uncertainty of the mean ocean sink over the 90s, which is taken as a reference (± [0.2-0.4] PgC/yr).

| Methods | | Periods | | | |
|-------------------|---------------|-------------|-------------|-------------|-------------|
| | | 1990s | 2000s | 2010s | 2019 |
| CMEMS-LSCE-FFNNv2 | Contemporary | 1.36 ± 0.12 | 1.55 ± 0.11 | 2.14 ± 0.12 | 2.63 ± 0.12 |
| | Anthropogenic | 2.20 ± 0.12 | 2.40 ± 0.11 | 3.01 ± 0.12 | 3.51 ± 0.13 |
| GCB2020* | | 2.0 ± 0.5 | 2.1 ± 0.5 | 2.5 ± 0.6 | 2.6 ± 0.6 |

Table 5: Air-sea CO₂ flux (PgC/yr) integrated over the global ocean. Comparison between CMEMS-LSCE-FFNNv2 and other estimates for periods in 1985-2020 (*source: Friedlingstein et al. 2020). The estimates of CMEMS-LSCE-FFNNv2 anthropogenic flux were computed by adjusting the contemporary flux estimates with the global ocean area of 361,900,000 km² and the riverine flux of 0.78 PgC/yr.

The map of average air-sea fluxes of CO₂ for the period 1985-2020 (Figure 6) highlights the regional variability of fluxes over the global ocean (top) and the coastal regions (bottom). Outgassing of CO₂ is associated with the upwelling of CO₂-rich subsurface waters (e.g., Equatorial Pacific). The northern and southern mid to high latitudes are sink regions. The North Atlantic stands out as a major area of CO₂ uptake explained by a marked strong cooling in winter and a vigorous phytoplankton bloom in spring and early summer. A region of enhanced uptake is also associated with the subtropical convergence zone in the southern hemisphere. Based on the gas exchange formulation the uncertainties derived from the 100-member ensemble of fgco2 estimates can be interpreted as the scalar product of the spco2 uncertainties resulted from the CMEMS-LSCE-FFNNv2 and the gas transfer coefficients ($k\rho L(1-f_{sea\ ice})$). Shown on the right panels of Figure 6, the uncertainty at the Southern Ocean with strong and variable winds is higher than the other regions.

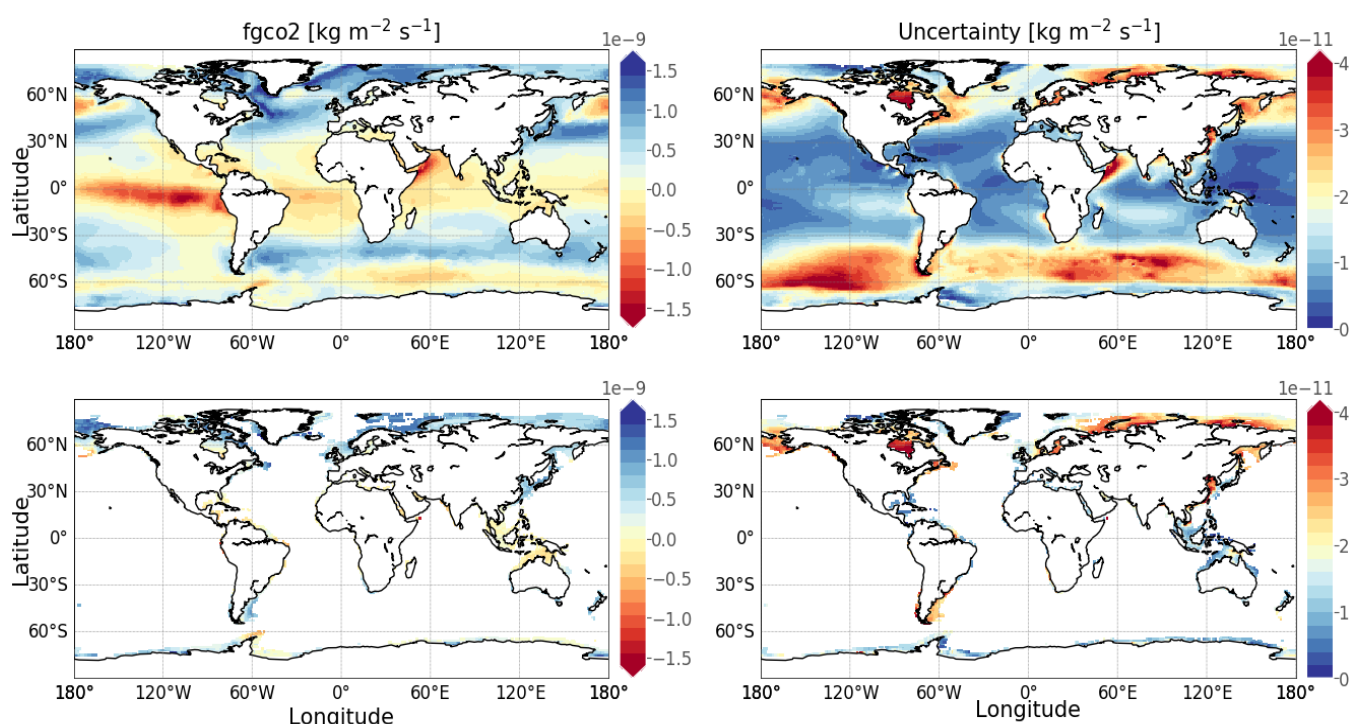


Figure 6. Reconstructed surface downward flux of carbon dioxide averaged over the global ocean (top) and coastal regions (bottom) for 1985 to 2020. Mean (left, positive values correspond to ocean uptake) and standard deviation (right) of the computed from the 100-member ensemble of CMEMS-LSCE-FFNNv2 are shown. The uncertainty estimate of the temporal mean per grid cell was corrected with a constant decorrelation length scale of 3 months.

The global yearly integrated air-sea flux of CO₂ seen in Figure 1 is characterized by interannual variability in response to modes of natural climate variability, which occurs superposed on the trend driven by increasing atmospheric CO₂ levels. The Equatorial Pacific is a dominant source of CO₂ to the atmosphere. Equatorial Pacific outgassing is strongly modulated by ENSO dynamics and imprints global air-sea fluxes of CO₂ (Feely et al., 2010). During El Niño events (e.g., 1997-1998, 2015-2016), reduced upwelling translates into reduced outgassing of CO₂ and an enhanced global ocean net air-sea CO₂ flux. To the contrary, La Niña events are characterized by increased upwelling, enhanced outgassing and a decreased global ocean net air-sea CO₂ flux (Chau et al. 2021 [Figure 9]).

IV.3 Surface ocean pH reconstruction

The assessment of the quality of the CMEMS-LSCE-FFNNv2 reconstruction with respect to pH data from the GLODAPv2.2021 bottle data set yields a global RMSD of 0.0348 pH and an absolute bias of 0.0193 pH units. Model scores for the regional assessment are shown in Table 6 and Figures 7, 8. CMEMS-LSCE-FFNNv2 produces reliable estimates of pH over the open ocean between “60°S-60°N”. Model errors (Figure 7) and uncertainty estimates (Figure 8) remain high over the coastal seas, continental shelves, and high latitudes.

| Region | Latitude boundaries | MAD | | RMSD | | r ² | |
|---|---------------------|--------|---------|--------|---------|----------------|---------|
| | | Open | Coastal | Open | Coastal | Open | Coastal |
| Global (10213, 600) | | 0.0173 | 0.0531 | 0.0296 | 0.0836 | 0.61 | 0.41 |
| Subpolar Atlantic (1137, 244) | 49°N to 76°N | 0.0281 | 0.0339 | 0.0450 | 0.0523 | 0.29 | 0.34 |
| Subpolar Pacific (403, 203) | 49°N to 76°N | 0.0409 | 0.0930 | 0.0644 | 0.1242 | 0.30 | 0.37 |
| Equatorial Pacific (1171, 1) | 18°S to 18°N | 0.0129 | 0.0130 | 0.0200 | 0.0130 | 0.65 | NaN |
| South Pacific (710, 0) | 44°S to 18°S | 0.0130 | NaN | 0.0157 | NaN | 0.80 | NaN |
| Southern Ocean (1465, 33) | 90°S to 44°S | 0.0169 | 0.0326 | 0.0245 | 0.0499 | 0.54 | 0.28 |

Table 6: Statistical validation for CMEMS-LSCE-FFNNv2 over the period 1985-2020. The assessment is based on the comparison between reconstructed surface ocean pH and pH values from GLODAPv2 bottle data set over the period 1985-2020. Global statistics and regional examples (Figure 3), number of GLODAPv2.2021 data per (open, coastal) region between brackets.

Reconstructed surface ocean pH is given on total H⁺ scale. Low pH values are found in upwelling regions (e.g., Equatorial Pacific, Arabian Sea) where old naturally dissolved inorganic carbon (DIC) enriched waters reach the surface ocean. Higher values are found in subpolar and polar waters, especially during spring and summer when photosynthesis draws DIC down (Figure 7). The uncertainty map of pH displayed on the right plot of Figure 7 is derived through a monthly uncertainty propagation for each member of 100-ensemble of spco2 following Orr et al. (2018) and the speciation software CO2sys (Lewis and Wallace, 1998; Van Heuven et al., 2011) (see II.2.c for details). Estimates of spco2 and associated uncertainties (see Figure 4) have the largest impact on the estimation of pH uncertainties.

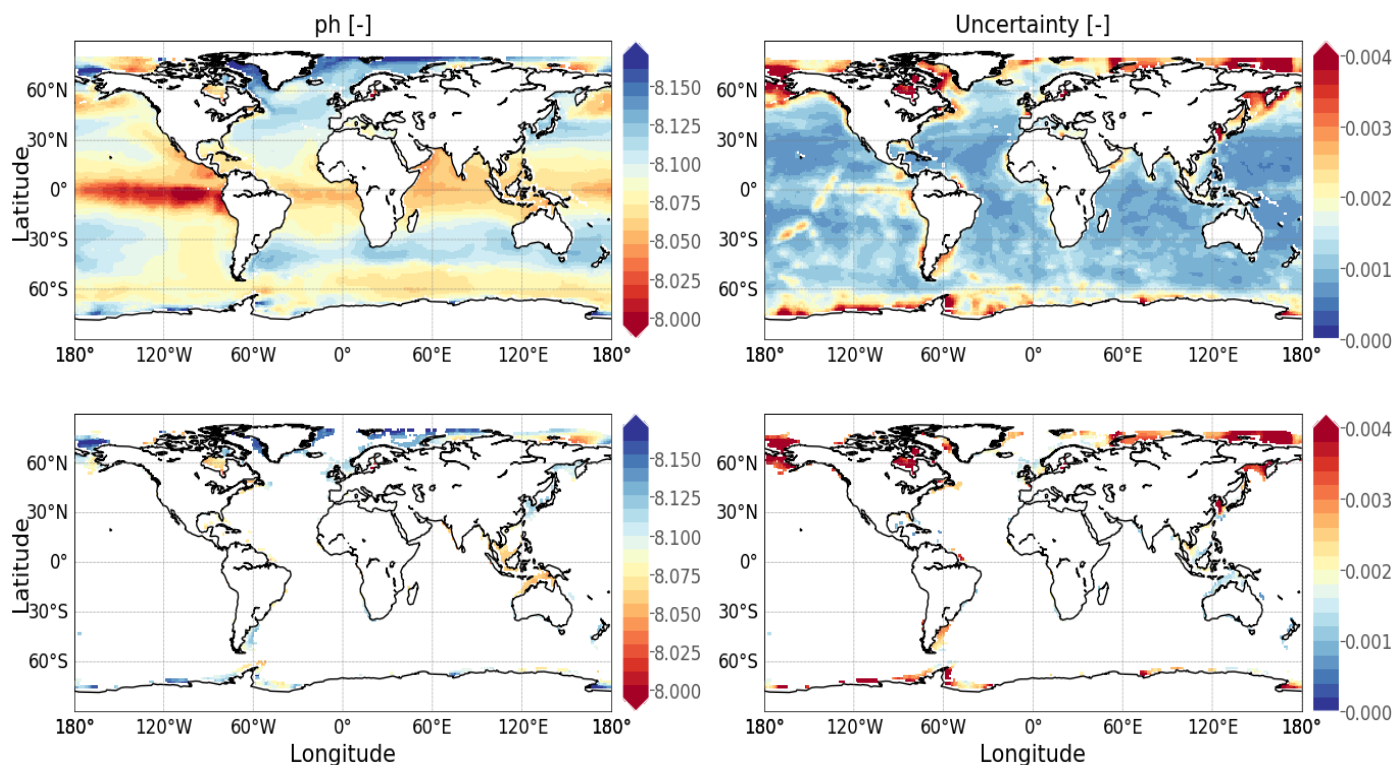


Figure 7. Reconstructed surface ocean pH averaged over the global ocean (top) and coastal regions (bottom) for 1985 to 2020. pH estimate (left) and uncertainty (right) computed for the 100-member ensemble of CMEMS-LSCE-FFNNv2 are shown. The uncertainty estimate of the temporal mean per grid cell was corrected with a constant decorrelation length scale of 3 months.

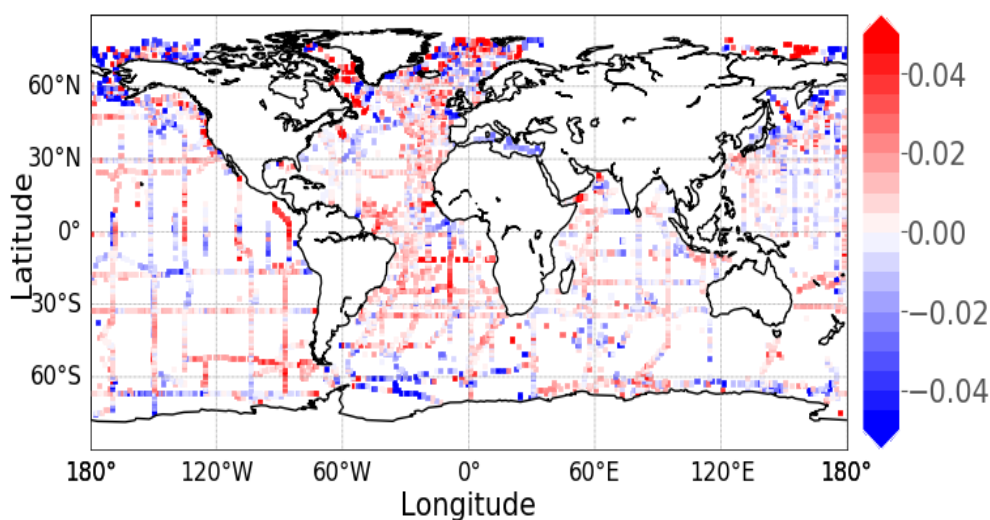


Figure 8. Maps of the mean of the differences between MULTIOBS pH and GLODAPv2.2021 bottle dataset.

V SYSTEM'S NOTICEABLE EVENTS, OUTAGES OR CHANGES

MULTIOBS_GLO_BIO_CARBON_SURFACE_REP_015_008 is the new name of MULTIOBS_GLO_BIO_REP_015_005.

This release corresponds to a reprocessed and extended time series of spco2, fgco2, ph. Estimates of spco2 are obtained from an ensemble of feed forward neural network (FFNNs) (Chau et al. 2021). It is referred to as CMEMS-LSCE-FFNNv2 and it is an improvement (method-wise) of the 1st version (LSCE-FFNN-v1) described in Denvil-Sommer et al. 2019. All variables are distributed with associated uncertainties derived from the 100-member ensemble.

Since the year 2021, the full CMEMS-LSCE-FFNN product including data over the coasts and high latitudes (above 60°N) has been submitted to CMEMS (and Global Carbon Project). Due to these changes, all statistics reported in this version of the document are significantly different from those in the previous version (2020). Note that the larger errors are derived from the reconstruction over the coasts and high latitudes. See Section IV and VI for further updates of the validation corresponding this new release.

VI QUALITY CHANGES SINCE PREVIOUS VERSION

Skill scores are improved for this release, CMEMS-LSCE-FFNNv2 (2021), as documented for spco2 (Table 7) and ph (Table 8). In comparison to the reconstruction skill of the LSCE-FFNN-v1 using K-fold cross-validation over the period 2001-2016 (Denvil-Sommer et al. 2019), CMEMS-LSCE-FFNNv2 provides spco2 estimates with less errors and higher correlation to the observations for the global ocean and the majority of regions. Taking advantage of an increase in the number of observations available in SOCATv2021, CMEMS-LSCE-FFNNv2 (2021) slightly improves the reconstruction of spco2 compared to the model run in 2020. In addition, the new release results in pH estimates with similar skill scores as those of the previous year (Table 8).

| Region | Latitude boundaries | MAD (Pa) | | | RMSD (Pa) | | | r ² | | |
|---|---------------------|----------|-------------|-------------|-----------|-------------|-------------|----------------|-------------|-------------|
| | | v1* | v2 (2020) | v2 (2021) | v1* | v2 (2020) | v2 (2021) | v1* | v2 (2020) | v2 (2021) |
| Global (300363, 321848) | | 1.17 | 1.04 | 1.04 | 1.82 | 1.68 | 1.68 | 0.76 | 0.76 | 0.76 |
| Subpolar Atlantic (36483, 39454) | 49°N to 76°N | 1.52 | 1.12 | 1.12 | 2.53 | 1.88 | 1.88 | 0.76 | 0.71 | 0.71 |
| Subpolar Pacific (14394, 15720) | 49°N to 76°N | 2.34 | 2.08 | 2.07 | 3.52 | 3.09 | 3.08 | 0.65 | 0.62 | 0.62 |
| Equatorial Pacific (45806, 48151) | 18°S to 18°N | 1.05 | 1.03 | 1.05 | 1.59 | 1.73 | 1.74 | 0.79 | 0.79 | 0.79 |
| South Pacific (18255, 19672) | 44°S to 18°S | 0.95 | 0.75 | 0.74 | 1.37 | 1.11 | 1.09 | 0.63 | 0.73 | 0.74 |
| Southern Ocean (34158, 37558) | 90°S to 44°S | 1.21 | 1.07 | 1.06 | 1.76 | 1.57 | 1.57 | 0.58 | 0.55 | 0.55 |

Table 7: Comparison between LSCE-FFNN-v1 and CMEMS-LSCE-FFNNv2 for reconstruction of surface ocean spco2 over the period 2001-2016. The assessment is on spco2 values from SOCAT data that are not used during algorithm training (*source of LSCE-FFNN-v1 using SOCATv5: Denvil-Sommer et al., 2019, units modified). Global statistics and regional examples (Figure 3), total number of SOCAT measurements (v2020, v2021) used in training CMEMS-LSCE-FFNNv2 (2020, 2021) per region between brackets.

For a comparison with CMEMS-LSCE-FFNNv2 (2020) over the full period, CMEMS-LSCE-FFNNv2 (2021) learned on the SOCATv2021 data, and hence benefitting with an increase in the number of observations in recent years, results in spco2 estimates with slightly lower RMSD (Figures 9). Additional observations with high values of spco2 possibly lead to a higher estimate of the new monthly spco2 timeseries as seen in Figure 10. Consequently, the global ocean Carbon sink and surface pH estimated by CMEMS-LSCE-FFNNv2 (2021) are lower than those estimated by the CMEMS-LSCE-FFNNv2 (2020) in the last two decades.

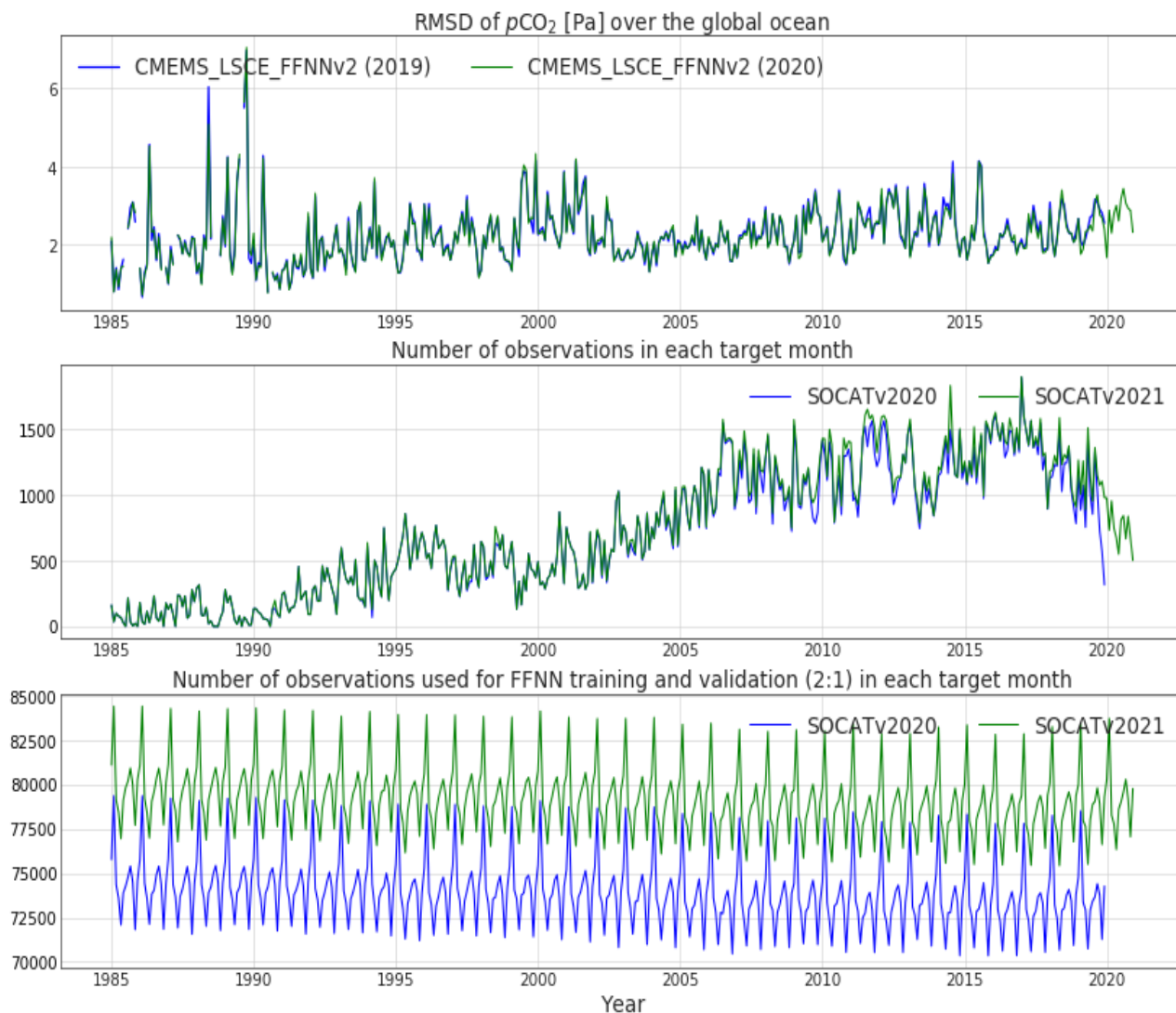


Figure 9. Top: RMSD of reconstructed global mean monthly surface ocean carbon dioxide partial pressure. Middle: Number of observations of monthly SOCAT data. Bottom: Number of observations of monthly SOCAT data used for fitting CMEMS-LSCE-FFNNv2 models.

| | MAD | | RMSD | | r ² | |
|---------------|---------------|---------------|---------------|---------------|----------------|---------------|
| | v2 (2020) | v2 (2021) | v2 (2020) | v2 (2021) | v2 (2020) | v2 (2021) |
| Global | 0.0157 | 0.0157 | 0.0253 | 0.0253 | 0.6410 | 0.6416 |

Table 8: Comparison of reconstructed pH data derived from spco2 of CMEMS-FFNN-LSCEv2 (2020, 2021) for global open ocean. The statistical assessment is based on the comparison between reconstructed surface ocean pH and pH values from GLODAPv2.2021 bottle data set over the common period 1985-2019.

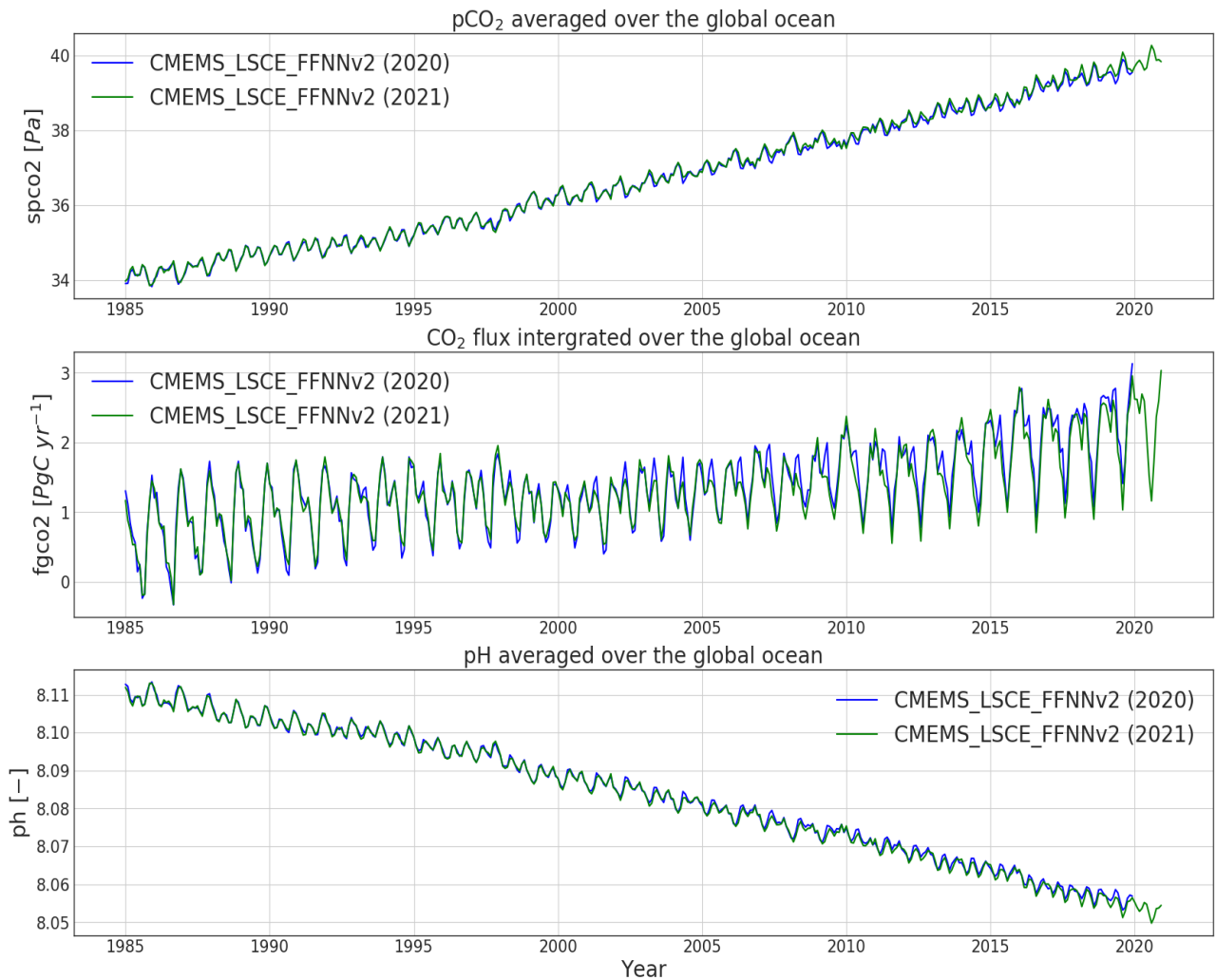


Figure 10. Global mean monthly surface ocean carbon dioxide partial pressure (top), monthly integration of air-sea fluxes (middle), and global mean monthly pH (bottom) estimated by CMEMS-LSCE-FFNNv2 (2020, 2021).

VII REFERENCES

Bakker, D. C. E., Pfeil, B., Landa, C. S., Metzl, N., O'Brien, K. M., Olsen, A., Smith, K., Cosca, C., Harasawa, S., Jones, S. D., Nakaoka, S.-I. et al.: A multi-decade record of high-quality fCO₂ data in version 3 of the Surface Ocean CO₂ Atlas (SOCAT), *Earth Syst. Sci. Data*, 8, 383–413, <https://doi.org/10.5194/essd-8-383-2016>, 2016.

Carter, B. R., Williams, N. L., Gray, A. R., & Feely, R. A.: Locally interpolated alkalinity regression for global alkalinity estimation. *Limnology and Oceanography: Methods*, 14(4), 268-277, 2016.

Carter, B. R., Feely, R. A., Williams, N. L., Dickson, A. G., Fong, M. B., & Takeshita, Y.: Updated methods for global locally interpolated estimation of alkalinity, pH, and nitrate. *Limnology and Oceanography: Methods*, 16(2), 119-131, 2018.

Chau, T. T. T., Gehlen, M., and Chevallier, F.: A seamless ensemble-based reconstruction of surface ocean pCO₂ and air–sea CO₂ fluxes over the global coastal and open oceans, *Biogeosciences Discuss.*, <https://doi.org/10.5194/bg-2021-207>, in review, 2021.

Chevallier, F., M. Fisher, P. Peylin, S. Serrar, P. Bousquet, F.-M. Bréon, A. Chédin, and P. Ciais, 2005: Inferring CO₂ sources and sinks from satellite observations: method and application to TOVS data. *J. Geophys. Res.*, 110, D24309, doi:10.1029/2005JD006390.

Chevallier, F., P. Ciais, T. J. Conway, T. Aalto, B. E. Anderson, P. Bousquet, E. G. Brunke, L. Ciattaglia, Y. Esaki, M. Fröhlich, A.J. Gomez, A.J. Gomez-Pelaez, L. Haszpra, P. Krummel, R. Langenfelds, M. Leuenberger, T. Machida, F. Maignan, H. Matsueda, J. A. Morguí, H. Mukai, T. Nakazawa, P. Peylin, M. Ramonet, L. Rivier, Y. Sawa, M. Schmidt, P. Steele, S. A. Vay, A. T. Vermeulen, S. Wofsy, D. Worthy, 2010: CO₂ surface fluxes at grid point scale estimated from a global 21-year reanalysis of atmospheric measurements. *J. Geophys. Res.*, 115, D21307, doi:10.1029/2010JD013887

Chevallier, F., 2013: On the parallelization of atmospheric inversions of CO₂ surface fluxes within a variational framework. *Geosci. Model. Dev.*, 6, 783-790, doi:10.5194/gmd-6-783-2013.

Denvil-Sommer, A., Gehlen, M., Vrac, M., and Mejia, C.: LSCE-FFNN-v1: a two-step neural network model for the reconstruction of surface ocean pCO₂ over the global ocean. *Geoscientific Model Development*, 12(5), 2091-2105, 2019.

Fay, A.R., McKinley, G.A., and Lovenduski, N.S.: Southern Ocean carbon trends: Sensitivity to methods, *Geophys. Res. Lett.*, 41, 6833–6840, doi:10.1002/2014GL061324, 2014.

Feely, R.A., Wanninkhof, R., Takahashi, T. and Tans, P.: Influence of El Niño on the equatorial Pacific contribution to atmospheric CO₂ accumulation. *Nature*, 398, 597-601.

Friedlingstein, P., O'Sullivan, M., Jones, M. W., Andrew, R. M., Hauck, J., Olsen, A., Peters, G. P., Peters, W., Pongratz, J., Sitch, S., Le Quéré, C., Canadell, J. G., Ciais, P., Jackson, R. B., Alin, S., Aragão, L. E. O. C., Arneeth, A., Arora, V., Bates, N. R., Becker, M., Benoit-Cattin, A., Bittig, H. C., Bopp, L., Bultan, S., Chandra, N., Chevallier, F., Chini, L. P., Evans, W., Florentie, L., Forster, P. M., Gasser, T., Gehlen, M., Gilfillan, D., Gkritzalis, T., Gregor, L., Gruber, N., Harris, I., Hartung, K., Haverd, V., Houghton, R. A., Ilyina, T., Jain, A. K., Joetzjer, E., Kadono, K., Kato, E., Kitidis, V., Korsbakken, J. I., Landschützer, P., Lefèvre, N., Lenton, A., Lienert, S., Liu, Z., Lombardozzi, D., Marland, G., Metzl, N., Munro, D. R., Nabel, J. E. M. S., Nakaoka, S.-I., Niwa, Y., O'Brien, K., Ono, T., Palmer, P. I., Pierrot, D., Poulter, B., Resplandy, L., Robertson, E., Rödenbeck, C., Schwinger, J., Séférian, R., Skjelvan, I., Smith, A. J. P., Sutton, A. J., Tanhua, T., Tans, P. P., Tian, H., Tilbrook, B., van der Werf, G., Vuichard, N., Walker, A. P., Wanninkhof, R., Watson, A. J., Willis,

D., Wiltshire, A. J., Yuan, W., Yue, X., and Zaehle, S.: Global Carbon Budget 2020, *Earth Syst. Sci. Data*, 12, 3269–3340, <https://doi.org/10.5194/essd-12-3269-2020>, 2020.

Gurney, K., Baker D., Rayner, P. and Denning S.: Interannual variations in continental-scale net carbon exchange and sensitivity to observing networks estimated from atmospheric CO₂ inversions for the period 1980 to 2005. *Global Biogeochemical Cycles*, 22, GB3025, 2008.

Hauck J., Zeising M., Le Quere C., Gruber N., Bakker D. C., Bopp L., Chau T. T. T., Gürses O., Ilyina T., Landschützer P., Lenton A., Resplandy L., Rödenbeck C., Schwinger J., Se R.: Consistency and challenges in the ocean carbon sink estimate for the Global Carbon Budget, *J. Front. Mar. Sci. - Ocean Observation*, doi: 10.3389/fmars.2020.571720, 2020.

Iida, Y., Kojima, A., Takatani, Y., Nakano, T., Midorikawa, T., and Ishii, M.: Trends in pCO₂ and sea-air CO₂ flux over the global open oceans for the last two decades, *J. Oceanogr.*, 71, 637–661, doi:10.1007/s10872-015-0306-4, 2015.

Landschützer, P., Gruber, N. and Bakker, D.C.E.: Decadal variations and trends of the global ocean carbon sink, *Global Biogeochemical Cycles*, 30, 1396-1417, doi:10.1002/2015GB005359, 2016

Landschützer, P., Gruber, N., Haumann, A., Rödenbeck, C., Bakker, D. C. E., van Heuven, S., Hoppema, M., Metzl, N., Sweeney, C., Takahashi, T., Tilbrook, B., and Wanninkhof, R.: The reinvigoration of the Southern Ocean carbon sink, *Science*, 349, 1221–1224, <https://doi.org/10.1126/science.aab2620>, 2015.

Laruelle, G. G., Dürr, H. H., Lauerwald, R., Hartmann, J., Slomp, C. P., Goossens, N., and Regnier, P.: Global multi-scale segmentation of continental and coastal waters from the watersheds to the continental margins, *Hydrol. Earth Syst. Sci.*, 17, 2029–2051, doi:10.5194/hess-17-2029-2013, 2013.

Laruelle, G. G., Landschützer, P., Gruber, N., Tison, J.-L., Delille, B., and Regnier, P.: Global high-resolution monthly pCO₂ climatology for the coastal ocean derived from neural network interpolation, *Biogeosciences*, 14, 4545–4561, 2017.

Lauvset, S. K., Lange, N., Tanhua, T., Bittig, H. C., Olsen, A., Kozyr, A., Álvarez, M., Becker, S., Brown, P. J., Carter, B. R., Cotrim da Cunha, L., Feely, R. A., van Heuven, S., Hoppema, M., Ishii, M., Jeansson, E., Jutterström, S., Jones, S. D., Karlsen, M. K., Lo Monaco, C., Michaelis, P., Murata, A., Pérez, F. F., Pfeil, B., Schirnack, C., Steinfeldt, R., Suzuki, T., Tilbrook, B., Velo, A., Wanninkhof, R., Woosley, R. J., and Key, R. M.: An updated version of the global interior ocean biogeochemical data product, GLODAPv2.2021, *Earth Syst. Sci. Data Discuss.* [preprint], <https://doi.org/10.5194/essd-2021-234>, in review, 2021.

Lewis, E., Wallace, D., & Allison, L. J.: Program developed for CO₂ system calculations (No. ORNL/CDIAC-105). Brookhaven National Lab., Dept. of Applied Science, Upton, NY (United States); Oak Ridge National Lab., Carbon Dioxide Information Analysis Center, TN (United States), 1998.

Menemenlis, D., Campin, J., Heimbach, P., Hill, C., Lee, T., Nguyen, A., Schodlok, M., and Zhang, H.: ECCO2: High resolution global ocean and sea ice data synthesis, *Mercator Ocean, Quarterly Newsletter*, 31, 13–21, 2008.

Orr, J.C., J.-M. Epitalon, A. G. Dickson, and J.-P. Gattuso (2018) Routine uncertainty propagation for the marine carbon dioxide system, in prep. for *Mar. Chem.*, in press, <http://doi.org/10.1016/j.marchem.2018.10.006>.

Resplandy, L., Keeling, R. F., Rödenbeck, C., Stephens, B. B., Khatiwala, S., Rodgers, K. B., Long, M. C., Bopp, L. and Tans, P. P.: Revision of global carbon fluxes based on a reassessment of oceanic and riverine carbon transport. *Nature Geoscience*, 11(7), p.504, 2018.

Rödenbeck, C., Bakker, D. C. E., Metzl, N., Olsen, A., Sabine, C., Cassar, N., Reum, F., Keeling, R. F., and Heimann, M.: Interannual sea-air CO₂ flux variability from an observation-driven ocean mixed-layer scheme, *Biogeosciences*, 11, 4599–4613, doi:10.5194/bg-11-4599-2014, 2014.

Rödenbeck, C., Bakker, D. C. E., Gruber, N., Iida, Y., Jacobson, A. R., Jones, S., Landschützer, P. et al.: Data-based estimates of the ocean carbon sink variability—first results of the Surface Ocean pCO₂ Mapping intercomparison (SOCOM), *Biogeosciences*, 12, 7251–7278, <https://doi.org/10.5194/bg-12-7251-2015>, 2015.

Takahashi, T., Sutherland, S.C., Wanninkhof, R., Sweeney, C., Feely, R.A., Chipman, D.W., Hales, B., Friederich, G., Chavez, F., Sabine, C., et al.: Climatological mean and decadal change in surface ocean pCO₂, and net sea-air CO₂ flux over the global oceans, *Deep-Sea Res. II*, 56(8–10), 554–577, <https://doi.org/10.1016/j.dsr2.2008.12.009>, 2009.

van Heuven, S. M., Hoppema, M., Huhn, O., Slagter, H. A., & de Baar, H. J.: Direct observation of increasing CO₂ in the Weddell Gyre along the Prime Meridian during 1973–2008. *Deep Sea Research Part II: Topical Studies in Oceanography*, 58(25–26), 2613–2635, 2011.

Wanninkhof, R.: Relationship between wind speed and gas exchange over the ocean revisited, *Limnol. Oceanogr. Methods*, 12, doi:10.4319/lom.2014.12.351, 2014.

Weiss, R.: Carbon dioxide in water and seawater: the solubility of a non-ideal gas, *Mar. Chem.*, 2, 203–205, [https://doi.org/10.1016/0304-4203\(74\)90015-2](https://doi.org/10.1016/0304-4203(74)90015-2), 1974.

World Ocean Atlas 2013 Product Documentation. T. Boyer, Ed.; A. Mishonov, Technical Ed.; 14 pp.